Isomerism and Structural Fluxionality in the Au_{26} and Au_{26}^- Nanoclusters

Bastian Schaefer,[†] Rhitankar Pal,[‡] Navneet S. Khetrapal,[§] Maximilian Amsler,[†] Ali Sadeghi,[†] Volker Blum,[⊥] Xiao Cheng Zeng,[§,*] Stefan Goedecker,[†,*] and Lai-Sheng Wang[∥,*]

[†]Department of Physics, University of Basel, Klingelbergstrasse 82, CH-4056 Basel, Switzerland, [‡]Department of Chemistry, Yale University, New Haven, Connecticut 06511, United States, [§]Department of Chemistry, University of Nebraska—Lincoln, Lincoln, Nebraska 68588, United States, [⊥]MEMS Department and Center for Materials Genomics, Duke University, Durham, North Carolina 27708, United States, and [∥]Department of Chemistry, Brown University, Providence, Rhode Island 02912, United States

ABSTRACT Using the minima hopping global optimization method at the density functional level, we found low-energy nanostructures for neutral Au_{26} and its anion. The local-density and a generalized gradient approximation of the exchange—correlation functional predict different nanoscale motifs. We found a vast number of isomers within a small energy range above the respective putative global minima with each method. Photoelectron spectroscopy of Au_{26}^- under different experimental conditions revealed definitive evidence of the presence of multiple isomers, consistent with the theoretical predictions. Comparison between the experimental and simulated photoelectron spectra suggests that the photoelectron spectra of Au_{26}^- contain a mixture of three isomers, all of which are low-symmetry core—shell-type nanoclusters with a single internal Au atom. We present a disconnectivity graph for Au_{26}^- that has been computed completely at the density functional level. The transition states used to build this disconnectivity graph are complete enough to predict Au_{26}^- to have a possible fluxional shell, which facilitates the understanding of its catalytic activity.

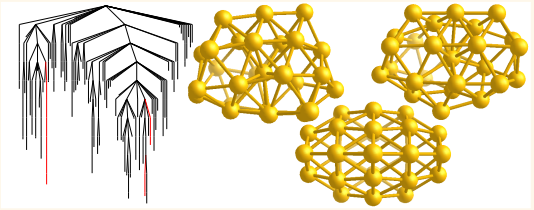

KEYWORDS: gold nanoclusters · minima hopping · density functional theory · photoelectron spectroscopy · BigDFT

Since bulk gold is the most inert metal, one could expect gold clusters to show no or only negligible chemical activity.[1,2] However, compared to bulk gold, the chemistry of gold nanoparticles is dramatically different, leading to promising and valuable properties for nanosciences such as nanoelectronics, nanobiology, and nanocatalysis.[3−8] In order to understand nanogold-related processes, size-selected gold clusters have been the focus of both theoretical and experimental investigations.[2,3,9−39] In particular, joint photoelectron spectroscopy (PES) and theoretical studies have elucidated the structures of anionic gold clusters over a wide size range.[2,19,23,34] For example, Au_{20}^- has been found to exhibit a tetrahedral pyramidal geometry,[19] and molecular dynamics (MD) simulations of Au_{34}^- suggest this cluster to have a fluxional shell, which could promise chemisorption.[2] Recently, Au_{36}^- to Au_{38}^- were shown to exhibit core—shell structures with a four-atom tetrahedral core.[39] Despite the successful previous work on gold clusters,[23,34,39] no theoretically predicted structure of Au_{26}^- has been experimentally confirmed so far. In order to close this gap, here we present the results of joint theoretical and PES study on this missing cluster. Besides presenting photoelectron (PE) spectra of Au_{26}^- under different experimental conditions, we carried out extensive structure predictions using the minima hopping[40−42] (MH) method and identified new global minimum candidates for both the neutral and anion systems. We use the comparison between theory and experiment for Au_{26}^- to identify energetically low-lying nanostructures that most probably exist in the experiment.

For the anionic system we also present a disconnectivity graph,[43] constructed from a database of connected minima and transition states that were computed using density functional theory (DFT). This database is complete enough to allow the prediction of chemical activity at finite temperatures. To our knowledge this is the first time that such a local map of the energy landscape has been computed completely at the DFT level.

* Address correspondence to xzeng1@unl.edu; stefan.goedecker@unibas.ch; lai-sheng_wang@brown.edu.

Received for review May 14, 2014 and accepted June 24, 2014.

Published online June 24, 2014
10.1021/nn502641q

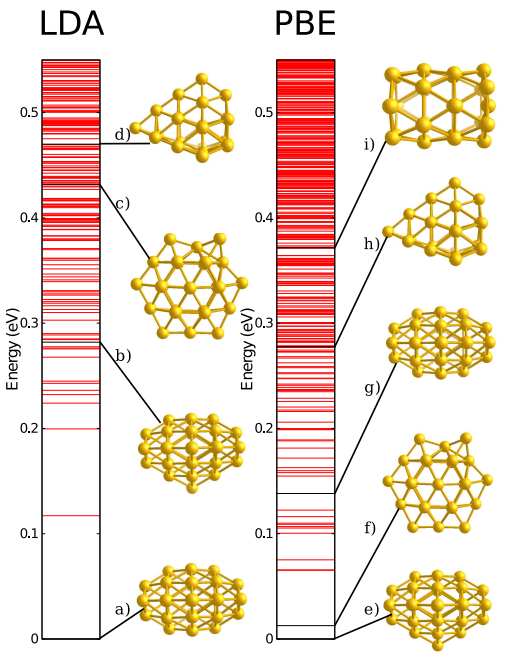

Figure 1. Energy spectra of the neutral Au_{26} based on the LDA and PBE functional. Shown are all minima with energy $\leq$ 0.55 eV. Depicted isomers are highlighted using black lines in the spectra, and when neglecting minor changes in the bond length, they are identical to their respective geometric counterparts of the other functional. Isomers (a), (b), (c) and (e), (f), (g) are the energetically lowest representatives we could find for each of their structural motifs. Isomer (a) [(g)] is a filled cage. According to the LDA functional, this filled cage is the putative global minimum. The PBE functional predicts isomer (e) [(b)], an empty cage, to be the putative global minimum. Isomers (d) [(h)] (pyramid) and (i) (tube) are previously claimed global minima[44,45] of the neutral Au_{26} cluster. The position of the tubular structure in the LDA spectrum is outside of the shown energy range.

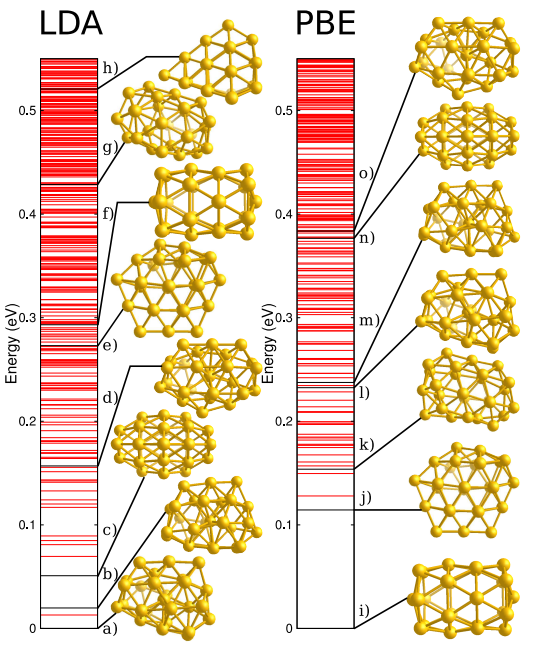

Figure 2. Same as Figure 1 but for the Au_{26}^- cluster. The computed PE spectra of the isomers (b), (c), and (d) [(m), (n), and (o)] can explain the experimentally measured PE spectrum very well (see below). Isomers (a), (e), (f), (g) and (i), (j), (k), (l) are the energetically lowest representatives we could find for each of their structural motifs. Isomers (a) and (e) [(l) and (j)] are the energetically lowest singly filled cage and hexagonal structures, respectively. Isomers (g) and (k) are the lowest empty cage structures; geometrically they are not identical. Isomers (f) [(i)] (tube) and (h) (pyramid) correspond to previously claimed global minima[44,45] of the neutral Au_{26} cluster. The position of the pyramidal structure in the PBE spectrum is outside of the shown energy range.

RESULTS AND DISCUSSIONS

Energy Landscape and Exchange–Correlation Functionals. Figures 1 and 2 show the energy spectra of local minima that were found during the MH runs within 0.55 eV of the respective global minima. We introduced four structural motifs: empty cages, cages filled with a single atom, the tubular cage, and hexagonal structures. The neutral and anionic systems possess the same motifs. Representatives for each motif can be found in Figure 3. As can be seen from the energy spectra, different functionals yield different energetic ordering for the structural motifs.

In the case of the anionic system we took a closer look at this circumstance. Figure 4a shows the energies of the five lowest energy configurations of each motif as obtained by the Perdew–Burke–Ernzerhof[46] (PBE) functional. Additionally, each configuration was relaxed using the local density approximation[47] (LDA), and the energies of corresponding configurations have been connected by lines. In the case of the tubular motif only one representative could be identified, and consequently only this single tube structure is shown.

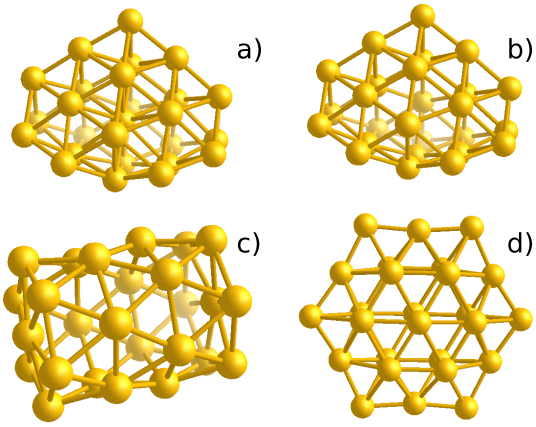

Figure 3. Representatives of the structural motifs. Isomer (a) represents the core–shell structure with a single internal atom, isomer (b) the empty cage, isomer (c) the high-symmetry tubular structure, and isomer (d) the hexagonal motif. These isomers also constitute a selection of starting configurations used for different minima hopping runs. Members of each motif may not necessarily be elements of the same point group as the shown representatives, but rather most configurations belong to the low-symmetry C_1 point group.

Figure 4a shows a significant energetic reordering of the motifs using different functionals. The LDA functional favors filled cages, whereas according to the PBE

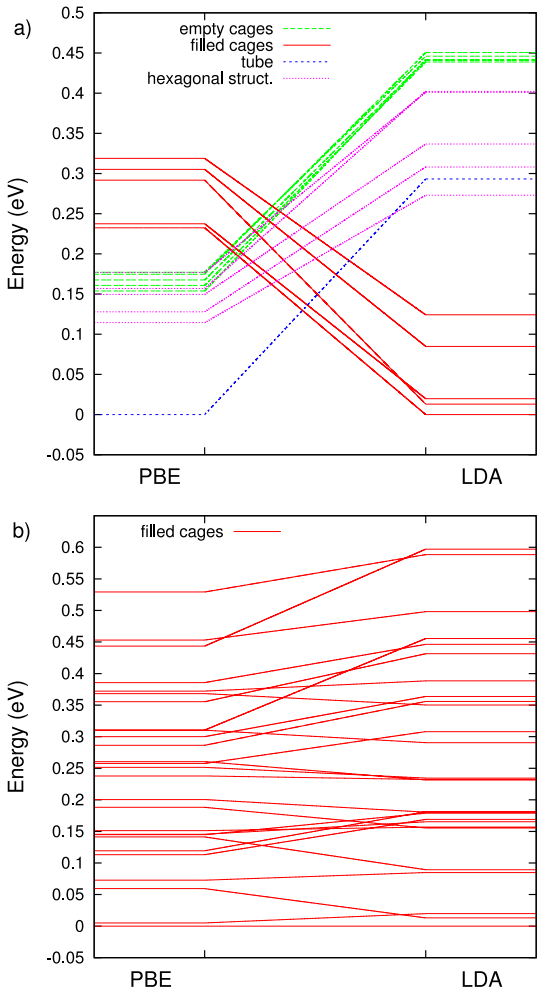

Figure 4. Energetic reordering of the Au_{26}^- minima using the PBE and LDA functionals. PBE and LDA energies of identical isomers are connected by lines. A significant reordering of motifs can be observed (a), whereas the overall energetic ordering within one motif is conserved (b). The energies in panel (a) are shifted with respect to the putative global minimum of each functional, whereas in panel (b) the energies are shifted such that the energy of the lowest energy filled cage isomer is zeroed.

functional, the same motif possesses a much higher energy. Figure 4b shows a more detailed plot of the energetic reordering of 25 configurations within the filled cage motif. Although both functionals produce a different energetic ordering, the overall ordering is conserved. This is in strong contrast to the energetic reordering of motifs.

In Figure 5 the potential energies of our local minima are plotted *versus* the permutationally optimized root-mean-square displacement (RMSD).[48] Both quantities are measured with reference to the respective putative global minimum. In particular when compared to systems like C_{60} or $B_{16}N_{16}$, Au_{26} and Au_{26}^- possess a vast number of structurally diverse minima within a small energy window above the putative global minimum.[49] This can also be seen from the energy spectra given in Figures 1 and 2. Using a Rosato–Guillopé–Legrand potential,

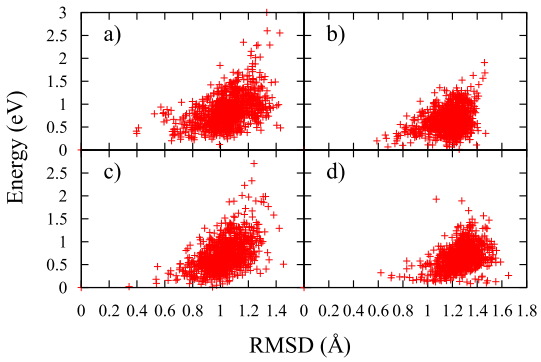

Figure 5. Potential energy *versus* permutationally optimized RMSD,[48] both measured with respect to the corresponding calculated lowest energy configuration. The upper plots show data for the neutral Au_{26} cluster using LDA (a) and PBE (b) functionals. The lower plots show data for the Au_{26}^- anion using LDA (c) and PBE (d) functionals.

Bao *et al.*[29] previously found similar results for large gold clusters. Considering the predictions of structurally different minima within a small energy range above the ground state by the two different exchange–correlation functionals and the Rosato–Guillopé–Legrand potential, it is conceivable that multiple isomers can also be observed experimentally. Indeed, numerous isomeric forms have been observed for some small gold cluster anions previously.[32–35,50] In the case of Au_{10}^-, at least three low-lying isomers were observed experimentally beside the global minimum.[50]

The vast number of structurally diverse minima that can be found in a comparably small energy range above the putative global minimum in conjunction with an exchange–correlation-functional-dependent energetic ordering of different structural motifs make Au_{26} and Au_{26}^- demanding systems for structure prediction. On one hand one cannot be sure to use the right exchange–correlation functional; on the other hand, more than one minimum may contribute to experimental results. Thus, when trying to identify configurations observed in experiment, it is advisible to introduce different structural motifs, if possible. Attention then should be focused on the first few energetically lowest configurations of each motif, instead of only the lowest energy structures. The complexity of the Au_{26}^- cluster was the major reason that it was omitted in previous joint PES and theoretical studies of medium-sized gold clusters.[23,34]

Computationally Predicted Low-Energy Configurations. *Neutral Cluster.* Next to the energy spectra of the neutral Au_{26} system (Figure 1) several specific configurations are visualized. Configurations (d) [(h)] (pyramidal structure) and (i) (tubular structure) have previously been proposed to be the global minimum[44,45] of Au_{26}. According to the LDA functional, the tubular structure is also a local minimum. However, its energy (~904 meV) is outside the energy range of Figure 1. The pyramidal structure can be obtained from the Au_{20} global minimum pyramid[19]

by adding six atoms to one face of the Au_{20} pyramid.[45] As shown by both LDA and PBE, we found a great number of configurations that are significantly lower in energy than the pyramidal configuration, even though the LDA and PBE functionals predict different sets of low-energy configurations. Among the 12 energetically lowest LDA configurations ($\lesssim$278 meV) only filled cages consisting of a single core atom surrounded by a 25-atom shell can be found. In contrast to this, empty cages and hexagonal structures are found among the energetically lowest structures of the PBE calculations.

The putative global minimum based on LDA calculations (Figure 1a) possesses C_{2v} symmetry and can be obtained from the pyramidal Au_{26} structure by removing the leftmost, uppermost, and lowermost (with respect to the illustration given in Figure 1d) corner atoms of the Au_{20} pyramidal part and attaching them to the right side of the illustration in Figure 1d. Another illustration of this isomer is given by configuration (a) of Figure 3. Only two further configurations (filled cages having C_1 and C_2 symmetry) were found in the energy region $\leq$ 200 meV.

The global minimum predicted by the PBE functional (Figure 1e) is a C_{2v} empty cage and can be constructed from configuration (a) [or (g)] of Figure 1 by removing the core atom and attaching it to the lowermost part of Figure 1a. Figure 3b shows this configuration from a different angle. In the region below 200 meV the PBE spectrum is considerably denser compared to the LDA spectrum. The first low-lying isomer (Figure 1f) is only 13 meV above the putative global PBE minimum. This structure is an isomer of the hexagonal motif with C_s symmetry. It is structurally considerably different from the putative global PBE minimum.

As mentioned above, not only the putative global minima (configurations (a) and (e) of Figure 1) should be taken into consideration when trying to identify the isomers experimentally. We suggest that the first few energetically lowest configurations of each of the motifs should be compared to future experimental results. Hence, we provide the coordinates of all configurations that can be found within 150 meV above the energetically lowest representative of each motif (but not less than five isomers) in the Supporting Information (SI). The structures given in the SI are sorted in ascending order with respect to their energy. For the sake of completeness, we also give the pyramidal and the tubular structure among the configurations in the SI.

Singly Charged Anion Cluster. Just as in the neutral case, the PBE and LDA functionals predict low-energy configurations belonging to different structural motifs for the anionic Au_{26}^- cluster (Figure 2).

At the LDA level, only cages being filled with a single atom are competing for the global minimum. The first nonfilled cage (Figure 2e) can be found at an energy of 273 meV. This isomer is of C_1 symmetry, but the hexagonal motif still can be recognized. The filled cage LDA global minimum (Figure 2a) also possesses C_1 symmetry.

The energetically lowest configuration predicted by the PBE functional is the tubular structure (isomer Figure 2i) with D_{6d} symmetry. The first low-lying isomer (Figure 2j) is identical to isomer (e) at the LDA level with only minor changes in bond lengths. In the energy region above the two low-lying isomers and below 232 meV, only empty cages and hexagonal structures are found. The putative global minimum at the LDA level (Figure 2a) is approximately 232 meV higher in energy at the PBE level (Figure 2l). Nevertheless, it is still the energetically lowest filled cage that was found.

As will be discussed in detail in subsequent sections, the computed PE spectra of the structures (b), (c), and (d) [(m), (n), and (o)] match very well with the experimental PE spectra. According to the LDA energy ordering, structure (b) is the third isomer, (c) is the fourth isomer, and (d) is the 18th isomer above the LDA global minimum. Henceforth these structures will be denoted as isomer 3, isomer 4, and isomer 18. The coordinates of the three identified structures are given in the SI.

In order to further assess the low-energy nature of isomers 3, 4, and 18 and the small energy window they can be found within, we have computed the energies of low-lying LDA isomers using SO-PBE0/CRENBL and M06/cc-pVDZ levels of theory as implemented in the NWChem 6.1.1 package.[51] The PBE0 functional (hybrid GGA[52]) and the M06 functional (hybrid meta-GGA[53]) are from higher rungs on "Jacob's ladder"[54] than the LDA and PBE functionals and thus are expected to give a good energy ranking. In particular the M06 and M06-L functionals have previously been shown to be accurate for gold clusters.[55,56] Table 1 shows the PBE0 and M06 energies in eV of the low-lying isomers together with their LDA energies (isomers 1−20 being core−shell structures with a single internal atom, isomers 65, 84, 101, 106, 126 being hexagonal, isomer 74 being tubular, and isomers 129, 175, 178, 185, 187 being empty cages). The LDA energies are identical to those shown in Figure 2. The relative energies of the core−shell isomers 3 and 4 are consistently found to be very low (within 0.15 eV) at all three levels of calculation. The energy of isomer 18 was found to be ~0.3 eV at PBE0, but ~0.14 eV using the M06 functional, which corresponds well with the ~0.16 eV predicted by the LDA functional. The relative energy of the previously proposed tubular isomer 74 was consistently found to be more than 0.2 eV higher than the putative global minimum. Furthermore, the predictions for the energetic ordering of the different motifs at the LDA, PBE0, and M06 levels of theory are found to be in good agreement with each other. It is worth emphasizing that the PBE functional, which usually gives better

TABLE 1. Relative Energies (in eV) of Au_{26}^- Isomers of All the Motifs[a]

Iso.	A	B	C	Iso.	A	B	C
1	0.00	0.08	0.00	17	0.16	0.26	0.19
2	0.01	0.15	0.07	18	0.16	0.32	0.14
3	0.02	0.00	0.01	19	0.16	0.20	0.17
4	0.05	0.14	0.15	20	0.17	0.26	0.20
5	0.07	0.33	0.22	65	0.27	0.17	0.35
6	0.08	0.29	0.16	74	0.29	0.21	0.21
7	0.08	0.19	0.06	84	0.31	0.16	0.37
8	0.09	0.26	0.15	101	0.34	0.18	0.37
9	0.12	0.17	0.08	106	0.34	0.32	–
10	0.12	0.17	0.21	126	0.37	0.24	0.42
11	0.12	0.09	0.08	129	0.37	0.23	0.43
12	0.13	0.32	0.26	175	0.43	0.44	–
13	0.14	0.23	0.18	178	0.44	0.34	–
14	0.14	0.19	0.13	185	0.44	0.35	–
15	0.14	0.05	0.22	187	0.44	0.41	–
16	0.15	0.31	0.24				

[a] The columns labeled with "Iso." give the isomer number, which follows the LDA ranking of Figure 2. Column A shows LDA energies of geometries relaxed at the LDA level (same as in Figure 2), column B shows SO-PBE0/CRENBL energies of geometries relaxed at the LDA level, and column C shows M06/cc-pVDZ energies of geometries relaxed at the M06/cc-pVDZ level.

atomization energies than the LDA functional, is not able to identify the correct structural motif.

Experimental Photoelectron Spectra. The PE spectrum of Au_{26}^- is shown in Figure 6a (magenta color). Numerous well-resolved PES bands are observed below ~5.4 eV binding energies, which should come mainly from Au 6s orbitals, whereas the more intense and almost continuous features above 5.4 eV should be due to the 5d band, according to previous PES studies.[23,34,57] Neutral Au_{26} is expected to be closed shell with a gap between its highest occupied (HOMO) and lowest unoccupied (LUMO) orbitals. The X band with a vertical detachment energy (VDE) of 3.46 ± 0.03 eV should correspond to electron detachment from the extra electron in Au_{26}^- that occupies the LUMO. The X′ band with a VDE of 3.75 ± 0.03 eV should correspond to electron detachment from the HOMO. However, the intensity of the X′ band is comparable to that of band X, and it seems too low to be from the HOMO. Instead, the X″ band with a VDE of 4.04 ± 0.03 eV appears to be the HOMO, suggesting that the X′ band should come from a different isomer of Au_{26}^- populated in the cluster beam.

Experimental evidence for this conjecture is provided by the PE spectrum of the Ar-tagged van der Waals complex $ArAu_{26}^-$ (black curve in Figure 6a), which should be in a colder condition than the bare Au_{26}^-. If normalized to the X band, the relative intensity of the X′ band and in fact all the higher binding energy bands seem to decrease under cold conditions. We also measured the PE spectrum of $Ar_2Au_{26}^-$

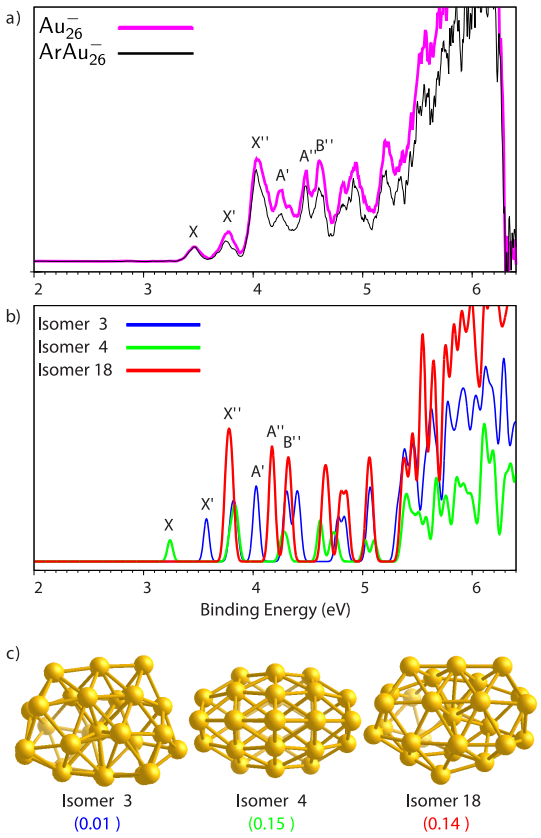

Figure 6. (a) Experimental PE spectra of Au_{26}^- (magenta) and $ArAu_{26}^-$ (black) at 193 nm (6.424 eV) photon energy; (b) simulated PE spectra from three isomers (3, 4, and 18) that best match the experimental spectra; (c) structures of the three isomers (all having core−shell structures with a single internal atom) and their relative energies (in eV) calculated at the M06/cc-pVDZ level of theory. The energies are shifted with respect to the computationally lowest energy isomer at the M06/cc-pVDZ level of theory (see Table 1). Isomer 3 is identical to Figure 2b, isomer 4 is identical to Figure 2c, and isomer 18 is identical to Figure 2d.

(not shown), which is similar to that of $ArAu_{26}^-$. This change of relative intensity between the X and X′ bands suggests that they come from two different isomers, and the X′ should come from a slightly higher free energy isomer so that its relative intensity is reduced at lower temperatures. Hence, the higher binding energy bands must be a mixture of detachment features from the two isomers. As will be seen below in comparison with the simulated density of states (DOS), bands X″, A″, and B″ also have contributions from a third isomer, whose first VDE contributes to band X″. The presence of at least three isomers experimentally for Au_{26}^- is consistent with the high density of low-lying isomers predicted computationally, making it an extremely challenging system to interpret.

Simulated Photoelectron Spectra of Low-Energy Isomers and Comparison with Experimental Spectrum. For each motif of Au_{26}^-, we simulated the PE spectra of several low-lying LDA geometries at the PBE0/CRENBL level of theory with the inclusion of spin−orbit (SO) effects. Plots of

these simulated spectra are given in Figure S1 (A−D) in the SI. At present there exists no mathematical rigorous and systematic method that would allow quantifying the similarity of two spectra, and therefore the best-matching spectra had to be chosen among all possible matches based on visual inspection and experience. As described above, there is concrete evidence for the existence of multiple isomers in the experimental spectra. Indeed, we found that no single isomer could fit all the observed PES features. As shown in Figure 6b, we have found that the combination of isomer 3 (blue), isomer 4 (green), and isomer 18 (red) results in a reasonable fit to the experimental spectra. Isomer 4 gives a very low first VDE of 3.2 eV, which is in good agreement with band X, but lower by ∼0.2 eV relative to the observed VDE of 3.46 eV. This difference is within the error of the calculated VDEs that we observed in previous studies.[23,32−35] The second band of isomer 4 is around 3.8 eV, giving rise to a HOMO−LUMO gap of ∼0.6 eV, similar to the gap between bands X″ and X, suggesting isomer 4 contributes to band X″. Higher binding energy features from isomer 4 are all overlapped with detachment features from other isomers. The first VDE of isomer 3 is at ∼3.55 eV, in good agreement with that of band X′, but again lower than the experimental VDE of band X′ by ∼0.2 eV. The third band of isomer 3 gives a VDE of ∼4 eV, giving rise to an energy difference of ∼0.5 eV between this third and the first band. This energy difference is in close agreement with the gap between bands A′ and X′. We noticed that the X″ band is quite strong, and it cannot be fully accounted for by the second detachment band from isomer 3 and isomer 4 alone. We found that isomer 18 gives a high first VDE at ∼3.8 eV, which is lower than the observed VDE of band X″ by ∼0.2 eV and could be a major contributor to this band. In fact, the second and third detachment transitions of isomer 18 are in good agreement with bands A″ and B″. Hence, only with the three isomers can we produce a good interpretation of the observed PE spectra for Au_{26}^-. The temperature dependence of the PE spectra suggests that isomer 4, which corresponds to band X, should be the lowest in free energy, whereas isomers 3 and 18 should be slightly higher in free energy because their relative PES intensities decreased when the cluster was colder. Theoretically (see Table 1) isomer 3 is predicted to be slightly lower in potential energy than isomer 4. However, due to low-temperature entropy effects and inaccuracies introduced by the exchange−correlation functional, a perfect one-to-one match between the experimentally observed (low temperature) free energy ordering and the theoretically computed (zero temperature) potential energy ordering cannot be expected.

Fluxional Character of Au_{26}^-. In order to estimate the transition rate out of a minimum across a transition state along a single reaction path, Eyring's transition state theory[58] can be used. In this theory the transition rate k_{mt} at temperature T out of a minimum m with energy E_m over a transition state t with energy E_t is given by

$$k_{mt} = \left(\frac{k_B T}{h}\right)\left(\frac{\bar{q}_t}{q_m}\right)\exp\left(-\frac{E_t - E_m}{k_B T}\right)$$

where $\bar{q}_t$ is the partition function of the transition state for coordinates normal to the reaction coordinate, q_m is the partition function of the minimum, k_B is the Boltzmann constant, and h is Planck's constant. For the calculation of the following rates, we assumed that the ratio of the partition functions in the above formula can be neglected since we are interested in rough order-of-magnitude estimates, only. At room temperature the transition rate across a barrier with an energy of 0.33 eV measured with respect to the corresponding minimum is roughly on the order of 10^7 s^{-1} and across a barrier of 0.13 eV roughly on the order of 10^{10} s^{-1}. At a temperature of 200 K the transition rates across the same barriers are roughly on the order of 10^4 s^{-1} and 10^9 s^{-1}, respectively.

Figure 7 shows a disconnectivity graph of Au_{26}^-. Two of the experimentally matched structures (isomers 3 and 18) are located in one of two different funnels, which merge in Figure 7 at the low energy of 0.33 eV. Due to only limited data available for this graph, we cannot rule out the existence of transition states that may merge these funnels at lower energies.

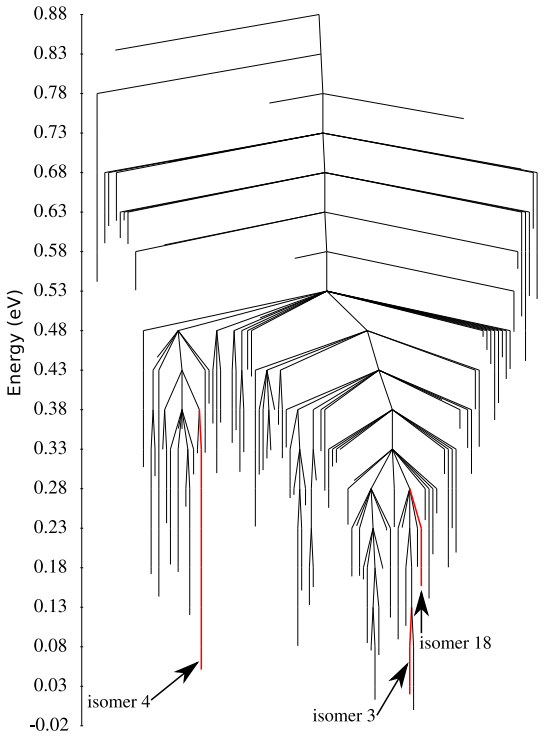

Figure 7. Disconnectivity graph of Au_{26}^- computed at the LDA level of theory. Energies are measured with respect to the putative global minimum (LDA).

Nevertheless, the transition states shown give an upper bound on the energetic height of existing transition pathways and thus allow estimating whether transitions out of a minimum can be observed on experimental time scales.

All the minima contained in the two funnels mentioned above can be interconverted into each other by crossing barriers not higher than 0.33 eV. For isomers 3 and 18 there even exist reaction paths to other minima with barriers lower than 0.13 eV. One therefore might expect that, in addition to isomers 3, 4, and 18, further isomers could exist in experiments. Indeed, we cannot exclude this possibility, as features of additional isomers might be buried under the strong peaks of the PE spectra of isomers 3, 4, and 18.

All structures in the stationary point database used to generate Figure 7 are core–shell structures with a single internal atom, and thus mainly atoms located in the shells of these structures are taking part in the just mentioned transitions. In this sense the shell of Au_{26}^- flows around the core atom and the cluster can be considered to be fluxional. In a previous[2] study it has been reasoned by means of an MD simulation that Au_{34}^- is fluxional, too. The fluxional property of clusters may promote catalytic, in particular chemisorptional, activities.

CONCLUSION

On the basis of a thorough *ab initio* exploration of the energy landscapes of Au_{26} and Au_{26}^-, we found that these systems possess a variety of structurally different but energetically similar minima. Many of the found structures are significantly lower in energy than previously suggested global minimum candidates, showing the importance of an unbiased global minimum search. On the basis of the analysis of the energy landscape and energetic reordering between the LDA and PBE functional we propose a set of new configurations for Au_{26} intended for comparing with future experimental results. Compared to systems with experimentally observable unique ground states,[49] both gold systems possess a large number of metastable structures within a small energy window above their computational putative global minima. Therefore, it is likely that a number of isomers can be found to coexist experimentally. By comparing the simulated PE spectra of a wide variety of isomers of Au_{26}^- with the experimental PE spectra at different conditions, we were able to identify three structures that can explain the experimental data reasonably. On the basis of a transition state search we concluded that Au_{26}^- may be a fluxional cluster system.

METHODS

Global Optimization. For global minimization of the potential energy surface the minima hopping method[40−42] coupled to the BigDFT code[59] was utilized. Beginning at a local minimum MH follows a short, random, and soft mode biased MD trajectory, at the end of which a local geometry optimization is performed. The minimum obtained by this optimization may or may not be identical to the minimum at the beginning of the MD trajectory. If it is not identical and its energy does not rise by more than a given threshold value compared to the energy of the current minimum, it is accepted to be the starting point of a subsequent MD trajectory. Both the kinetic energy of the MD part and the just mentioned energy threshold are adjusted by an energy feedback mechanism, which is based on the history of all visited minima. This feedback prevents the algorithm from getting stuck in low energy regions of coordinate space, and in addition to the use of soft mode biased[60] MD trajectories, it ensures that the Bell–Evans–Polanyi[61,62] principle is exploited. If the minimum that has been obtained by the above mentioned local optimization is identical to the one at the beginning of the MD trajectory, the threshold on the potential energy does not get modified and a new MD trajectory with an increased kinetic energy is started at the current minimum.

The global optimization was performed completely at the DFT level, which has shown to be more efficient for the present system size than performing a global minimum search on a force field or other less accurate methods and postrelaxing an energetically low-lying subset of configurations using DFT methods.[41]

For all local geometry optimizations a combination of conjugate gradient and a modified Broyden–Fletcher–Goldfarb–Shanno (BFGS) algorithm as implemented in BigDFT was used.

In order to predict the putative global minimum of the Au_{26} and Au_{26}^- potential energy landscapes, we split the computations into several steps. As the first step we performed MH runs on the energy landscape of the neutral Au_{26} using both standard LDA[47] and PBE[46] functionals in combination with the corresponding relativistic and norm-conserving Hartwigsen–Goedecker–Hutter (HGH) semicore pseudopotentials.[63,64]

For each functional several separate runs with different starting configurations were performed. A selection of the initial configurations is shown in Figure 3. The starting configurations were constructed manually or are from previous work, such as the tubular structure (Figure 3c), which was proposed to be the global minimum of Au_{26}.[44]

The BigDFT code uses a systematic wavelet basis set. The corresponding grid spacing and the spatial extension of the basis function were chosen such that a rotation of a whole cluster in the $\mathbb{R}^3$-space changed the energy by less than 10^{-4} hartree. For all MH runs geometry optimizations were stopped as soon as 20% of the force consisted of computational noise. On average, this happened when the largest force acting on any atom in a cluster was approximately 5×10^{-5} hartree/bohr in the case of the LDA functional and 3×10^{-4} hartree/bohr for PBE.

In the second step the minima of the LDA runs were postrelaxed by using the PBE functional and vice versa. Again we used parameters resulting in an energy accuracy better than 10^{-4} hartree and the largest force acting on any atom of approximately 5×10^{-5} hartree/bohr (LDA) and 3×10^{-4} hartree/bohr (PBE). The sets consisting of local minima from all the different runs were then merged by removing duplicates. Two sets of local minima were formed: one from LDA and the other from PBE calculations. Both sets were relaxed finally by treating the configurations as singly charged anions using both LDA and PBE functionals. Again, configurational duplicates that emerged in this relaxation process were removed. The parameters for the relaxations of the anions were chosen such that the energy changed by less than 10^{-4} hartree when rotating the configurations and the geometry optimizations were stopped

as soon as 33% of the force consisted of noise. For both functionals this happened when the largest force on any atom was approximately 5×10^{-5} hartree/bohr. In order to assess the accuracy of our BigDFT pseudopotential calculations, we compared the energetic ordering of several relaxed configurations with results obtained with the FHI-aims code.[65] The basis set used in the FHI-aims calculations was the extremely well converged "tier 2"[65] level with a large confinement radius (onset: 6 Å). Energies agreed within less than 3 meV per atom, showing that the pseudopotentials in the BigDFT calculations were highly accurate.

In total the above procedure resulted in roughly 900 distinct local minima for each of the four sets.

Computation of Transition States. If bond-breaking takes place, it is well known that the energies for transition states from DFT calculations using conventional exchange−correlation functionals are usually of poor quality.[66−68] For transitions involving only minor changes in the number of bonds, it has been argued by Zupan *et al.*[69] that there is little difference between GGA and LDA barriers, and thus both GGA and LDA should perform equally well in this case. Ghasemi *et al.* confirmed this by comparing the transition state energies of Si_8 resulting from LDA, PBE, and B3LYP calculations to diffusion Monte Carlo calculations.[70] They found that PBE and B3LYP are outperformed by the LDA functional. This result was explained by the fact that in contrast to the atoms of transition states of chemical reactions those of Si_8 are in a similar environment to the atoms of local minima. As a consequence, the transition states of Si_8 are difficult to distinguish from local minimum configurations by visual inspection. They concluded that DFT self-interaction errors are expected to cancel to a large degree, and highly inhomogeneous environments with large density gradients are not relevant for the calculation of the transitions states of the Si_8 cluster. For the current Au_{26}^- cluster, the situation is similar. We observed that in most cases only a local rearrangement of atoms took place when going over a transition state from one minimum to another. On the basis of visual inspection, it is almost impossible to distinguish a local minimum from a transition state. Additionally, in contrast to the PBE functional, the LDA functional is able to predict the experimentally observed Au_{26}^- structures as low-energy minima, and the LDA energies correlate very well with the energies obtained from the highly accurate, but computationally more demanding, M06 hybrid meta-GGA functional (see Table 1).[53] Furthermore, LDA is believed to describe the gold metallic bonds better than the PBE functional.[71] For fcc gold it has been shown that properties such as the lattice constant, phonon dispersion, and the equation of state are reproduced more accurately by the LDA functional than by PBE.[72−75] We therefore expect the LDA functional to give reasonable transition state energies for the Au_{26}^- system and decided to use this functional for the transition state search.

The transition state search was done for Au_{26}^- using the Bar−Saddle method.[76] This method efficiently identifies transition states located in between two input configurations. We started the transition state search in the vicinity of the experimentally identified Au_{26}^- clusters. The initial input configurations were chosen by searching among all found local minima for structures that are close to the experimentally identified structures. As a distance measure we used the permutationally optimized RMSD.[48] The transition states found in this way do not need to be connected directly to the input minima, so if required, the transition state search had to be repeated recursively until the two input minima were connected. In order to decide whether two minima are directly connected to a transition state, we performed a small step in the forward and backward direction of the negative mode at the transition state followed by a local geometry optimization. The minima and transition states that emerged during the above connection attempts form a stationary point database, which is visualized as a disconnectivity graph[43] using the disconnectionDPS[77] software. For minima that seemed to lie behind high energy barriers permutationally optimized RMSDs to all the other minima in the stationary point database were computed and connection attempts to the closest structures were performed. This procedure was iterated until 264 transition states connecting 118 minima were found. Due to the high computational cost of computing transition states, it was not possible to compute a significantly larger stationary point database. The size of our database is not large enough to ensure that the lowest lying paths among all of its minima have been found. However, for our purpose of finding upper bounds on the energy along transition paths, a fully converged disconnectivity graph is not necessary. Furthermore, during the addition of the last 50 transition states to the stationary point database, the disconnectivity graph did not show any significant changes.

On average, the relaxation of a transition state was stopped as soon as the largest component of the force acting on any atom was approximately 2×10^{-4} hartree/bohr.

Computation of Photoelectron Spectra. The electronic DOS for several MH algorithm-generated low-lying isomers of Au_{26}^- (typically within ~1.0 eV of the lowest energy isomer) were computed and used to compare with the experimental PE spectra. Single-point energy calculations of these low-lying structures were performed at the PBE0/CRENBL level of theory with the inclusion of spin−orbit effects as implemented in the NWChem 6.1.1 package.[51] Previous reports have shown that the inclusion of the SO effects yields almost quantitative agreement between the experimental PE spectra and computed DOS for gold clusters of various sizes and shapes.[34] The first VDEs of each isomer were calculated as the difference between the energies of the anionic and the corresponding neutral species at the anion geometry. The binding energies of the deeper occupied orbitals of the anion were then added to the first VDE to approximate higher binding energy features. Each computed peak was then fitted with Gaussian functions of 0.06 eV width to yield a computed PE spectrum, which was used to compare with the experimental spectra of Au_{26}^-.

Experimental Methods. The PES experiment was performed using a magnetic-bottle apparatus equipped with a laser vaporization supersonic cluster source and a time-of-flight mass analyzer.[78] A pulsed laser beam was focused onto a pure gold disk target, generating a plasma containing gold atoms. A high-pressure helium carrier gas pulse was delivered to the nozzle simultaneously, cooling the plasma and initiating nucleation. As shown previously,[79] by carefully controlling the resident time of the clusters in the nozzle, relatively cold and equilibrated clusters can be produced from our laser vaporization supersonic cluster source. The cooling effects have been confirmed recently by the observation of van der Waals complexes of gold cluster anions with Ar or O_2.[27,28,50] In the present study, relatively cold Au_{26}^- clusters were produced using a helium carrier gas seeded with 5% Ar. In addition, we were able to produce even colder Au_{26}^- complexed with Ar atoms, $Ar_nAu_{26}^-$ (n = 1, 2). The Au_{26}^- and $Ar_nAu_{26}^-$ clusters were selected by a mass gate and decelerated before being photodetached by a 193 nm laser beam from an ArF excimer laser. Photoelectrons were collected with a magnetic bottle at nearly 100% efficiency in a 3.5-m-long electron flight tube for kinetic energy analyses. The PE kinetic energies were calibrated by the known spectrum of Au^- and subtracted from the photon energy to obtain the reported electron binding energy spectra. The electron energy resolution was $\Delta E/E \approx 2.5\%$ (*i.e.*, 25 meV for 1 eV electrons).

Conflict of Interest: The authors declare no competing financial interest.

Acknowledgment. The theoretical work at the University of Basel was supported by a grant from the Indo Swiss Joint Research Programme (ISJRP) and by a grant from the Swiss National Supercomputing Centre (CSCS) under project ID s142. The experimental work was supported by the National Science Foundation (CHE-1049717 to L.S.W.). We thank Dr. Xi Li and Dr. Wei Huang for their assistance with the experiment.

Supporting Information Available: The computed PE spectra, the coordinates of isomers 3, 4, and 18 for Au_{26}^-, and the coordinates of low-energy isomers of each motif for Au_{26}. This material is available free of charge *via* the Internet at http://pubs.acs.org.

REFERENCES AND NOTES

1. Hammer, B.; Norskov, J. K. Why Gold is the Noblest of All the Metals. *Nature* **1995**, *376*, 238–240.
2. Gu, X.; Bulusu, S.; Li, X.; Zeng, X.; Li, J.; Gong, X.; Wang, L. S. Au_{34}^-: A Fluxional Core-Shell Cluster. *J. Phys. Chem. C* **2007**, *111*, 8228–8232.
3. Sanchez, A.; Abbet, S.; Heiz, U.; Schneider, W.-D.; Häkkinen, H.; Barnett, R. N.; Landman, U. When Gold is Not Noble: Nanoscale Gold Catalysts. *J. Phys. Chem. A* **1999**, *103*, 9573–9578.
4. Mirkin, C. A.; Letsinger, R. L.; Mucic, R. C.; Storhoff, J. J. A DNA-Based Method for Rationally Assembling Nanoparticles Into Macroscopic Materials. *Nature* **1996**, *382*, 607–609.
5. Alivisatos, A. P.; Johnsson, K. P.; Peng, X.; Wilson, T. E.; Loweth, C. J.; Bruchez, M. P.; Schultz, P. G. Organization of 'Nanocrystal Molecules' Using DNA. *Nature* **1996**, *382*, 609–611.
6. Chen, S. Gold Nanoelectrodes of Varied Size: Transition to Molecule-Like Charging. *Science* **1998**, *280*, 2098–2101.
7. Pyykkö, P. Theoretical Chemistry of Gold. *Angew. Chem., Int. Ed.* **2004**, *43*, 4412–4456.
8. Haruta, M. Size- and Support-Dependency in the Catalysis of Gold. *Catal. Today* **1997**, *36*, 153–166.
9. Cleveland, C.; Landman, U.; Schaaff, T.; Shafigullin, M.; Stephens, P.; Whetten, R. Structural Evolution of Smaller Gold Nanocrystals: The Truncated Decahedral Motif. *Phys. Rev. Lett.* **1997**, *79*, 1873–1876.
10. Garzón, I.; Michaelian, K.; Beltrán, M.; Posada-Amarillas, A.; Ordejón, P.; Artacho, E.; Sánchez-Portal, D.; Soler, J. Lowest Energy Structures of Gold Nanoclusters. *Phys. Rev. Lett.* **1998**, *81*, 1600–1603.
11. Bravo-Pérez, G.; Garzón, I.; Novaro, O. *Ab initio* Study of Small Gold Clusters. *J. Mol. Struct. Theochem* **1999**, *493*, 225–231.
12. Häkkinen, H.; Landman, U. Gold Clusters (Au_N, $2 \le N \le 10$) and Their Anions. *Phys. Rev. B* **2000**, *62*, R2287–R2290.
13. Furche, F.; Ahlrichs, R.; Weis, P.; Jacob, C.; Gilb, S.; Bierweiler, T.; Kappes, M. M. The Structures of Small Gold Cluster Anions as Determined by a Combination of Ion Mobility Measurements and Density Functional Calculations. *J. Chem. Phys.* **2002**, *117*, 6982–6990.
14. Gilb, S.; Weis, P.; Furche, F.; Ahlrichs, R.; Kappes, M. M. Structures of Small Gold Cluster Cations (Au_n^+, $n < 14$): Ion Mobility Measurements versus Density Functional Calculations. *J. Chem. Phys.* **2002**, *116*, 4094–4101.
15. Yoon, B.; Häkkinen, H.; Landman, U. Interaction of O_2 with Gold Clusters: Molecular and Dissociative Adsorption. *J. Phys. Chem. A* **2003**, *107*, 4066–4071.
16. Häkkinen, H.; Yoon, B.; Landman, U.; Li, X.; Zhai, H.-J.; Wang, L. S. On the Electronic and Atomic Structures of Small Au_N^- ($N = 4-14$) Clusters: A Photoelectron Spectroscopy and Density-Functional Study. *J. Phys. Chem. A* **2003**, *107*, 6168–6175.
17. Häkkinen, H.; Abbet, S.; Sanchez, A.; Heiz, U.; Landman, U. Structural, Electronic, and Impurity-Doping Effects in Nanoscale Chemistry: Supported Gold Nanoclusters. *Angew. Chem., Int. Ed.* **2003**, *42*, 1297–1300.
18. Lee, H. M.; Ge, M.; Sahu, B. R.; Tarakeshwar, P.; Kim, K. S. Geometrical and Electronic Structures of Gold, Silver, and Gold-Silver Binary Clusters: Origins of Ductility of Gold and Gold-Silver Alloy Formation. *J. Phys. Chem. B* **2003**, *107*, 9994–10005.
19. Li, J.; Li, X.; Zhai, H.-J.; Wang, L. S. Au_{20}: A Tetrahedral Cluster. *Science* **2003**, *299*, 864–867.
20. Fernández, E.; Soler, J.; Garzón, I.; Balbás, L. Trends in the Structure and Bonding of Noble Metal Clusters. *Phys. Rev. B* **2004**, *70*, 165403-1–165403-14.
21. Neumaier, M.; Weigend, F.; Hampe, O.; Kappes, M. M. Binding Energies of CO on Gold Cluster Cations Au_n^+ ($n = 1-65$): A Radiative Association Kinetics Study. *J. Chem. Phys.* **2005**, *122*, 104702-1–104702-11.
22. Lechtken, A.; Schooss, D.; Stairs, J. R.; Blom, M. N.; Furche, F.; Morgner, N.; Kostko, O.; von Issendorff, B.; Kappes, M. M. Au_{34}^-: A Chiral Gold Cluster? *Angew. Chem., Int. Ed.* **2007**, *46*, 2944–2948.
23. Bulusu, S.; Li, X.; Wang, L. S.; Zeng, X. C. Structural Transitions from Pyramidal to Fused Planar to Tubular to Core/Shell Compact in Gold Clusters: Au_n^- ($n = 21-25$). *J. Phys. Chem. C* **2007**, *111*, 4190–4198.
24. Jalbout, A. F.; Contreras-Torres, F. F.; Pérez, L. A.; Garzón, I. L. Low-Symmetry Structures of $Au_{32}Z$ ($Z = +1, 0, -1$) Clusters. *J. Phys. Chem. A* **2008**, *112*, 353–357.
25. Santizo, I. E.; Hidalgo, F.; Pérez, L. A.; Noguez, C.; Garzón, I. L. Intrinsic Chirality in Bare Gold Nanoclusters: The Au_{34}^- Case. *J. Phys. Chem. C* **2008**, *112*, 17533–17539.
26. Johansson, M.; Lechtken, A.; Schooss, D.; Kappes, M.; Furche, F. 2D-3D Transition of Gold Cluster Anions Resolved. *Phys. Rev. A* **2008**, *77*, 053202-1–053202-7.
27. Huang, W.; Wang, L. S. Probing the 2D to 3D Structural Transition in Gold Cluster Anions Using Argon Tagging. *Phys. Rev. Lett.* **2009**, *102*, 153401-1–153401-4.
28. Huang, W.; Bulusu, S.; Pal, R.; Zeng, X. C.; Wang, L. S. Structural Transition of Gold Nanoclusters: From the Golden Cage to the Golden Pyramid. *ACS Nano* **2009**, *3*, 1225–1230.
29. Bao, K.; Goedecker, S.; Koga, K.; Lançon, F.; Neelov, A. Structure of Large Gold Clusters Obtained by Global Optimization Using the Minima Hopping Method. *Phys. Rev. B* **2009**, *79*, 41405-1–41405-4.
30. Lechtken, A.; Neiss, C.; Kappes, M. M.; Schooss, D. Structure Determination of Gold Clusters by Trapped Ion Electron Diffraction: $Au_{14}^- - Au_{19}^-$. *Phys. Chem. Chem. Phys.* **2009**, *11*, 4344–4350.
31. Schooss, D.; Weis, P.; Hampe, O.; Kappes, M. M. Determining the Size-Dependent Structure of Ligand-Free Gold-Cluster Ions. *Philos. Trans. R. Soc., A* **2010**, *368*, 1211–1243.
32. Wang, L.-M.; Pal, R.; Huang, W.; Zeng, X. C.; Wang, L. S. Observation of Earlier Two-to-Three Dimensional Structural Transition in Gold Cluster Anions by Isoelectronic Substitution: MAu_n^- ($n = 8-11$; M=Ag,Cu). *J. Chem. Phys.* **2010**, *132*, 114306-1–114306-8.
33. Huang, W.; Pal, R.; Wang, L.-M.; Zeng, X. C.; Wang, L. S. Isomer Identification and Resolution in Small Gold Clusters. *J. Chem. Phys.* **2010**, *132*, 054305-1–054305-5.
34. Shao, N.; Huang, W.; Gao, Y.; Wang, L.-M.; Li, X.; Wang, L. S.; Zeng, X. C. Probing the Structural Evolution of Medium-Sized Gold Clusters: Au_n^- ($n = 27-35$). *J. Am. Chem. Soc.* **2010**, *132*, 6596–6605.
35. Pal, R.; Wang, L.-M.; Huang, W.; Wang, L. S.; Zeng, X. C. Structure Evolution of Gold Cluster Anions Between the Planar and Cage Structures by Isoelectronic Substitution: Au_n^- ($n = 13-15$) and MAu_n^- ($n = 12-14$; M = Ag, Cu). *J. Chem. Phys.* **2011**, *134*, 054306-1–054306-7.
36. Wang, L.-M.; Wang, L. S. Probing the Electronic Properties and Structural Evolution of Anionic Gold Clusters in the Gas Phase. *Nanoscale* **2012**, *4*, 4038–4053.
37. León, I.; Yang, Z.; Wang, L. S. High Resolution Photoelectron Imaging of Au_2^-. *J. Chem. Phys.* **2013**, *138*, 184304-1–184304-5.
38. Yang, Z.; León, I.; Wang, L. S. Communication: Vibrational Spectroscopy of Au_4 from High Resolution Photoelectron Imaging. *J. Chem. Phys.* **2013**, *139*, 021106-1–021106-4.
39. Shao, N.; Huang, W.; Mei, W.-N.; Wang, L. S.; Wu, Q.; Zeng, X. C. Structural Evolution of Medium-Sized Gold Clusters Au_n^- ($n = 36, 37, 38$): Appearance of Bulk-Like Face Centered Cubic Fragment. *J. Phys. Chem. C* **2014**, *118*, 6887–6892.
40. Goedecker, S. Minima Hopping: An Efficient Search Method for the Global Minimum of The Potential Energy Surface of Complex Molecular Systems. *J. Chem. Phys.* **2004**, *120*, 9911–9917.
41. Goedecker, S.; Hellmann, W.; Lenosky, T. Global Minimum Determination of the Born-Oppenheimer Surface within Density Functional Theory. *Phys. Rev. Lett.* **2005**, *95*, 55501-1–55501-4.
42. Schönborn, S. E.; Goedecker, S.; Roy, S.; Oganov, A. R. The Performance of Minima Hopping and Evolutionary Algorithms for Cluster Structure Prediction. *J. Chem. Phys.* **2009**, *130*, 144108-1–144108-9.

43. Becker, O. M.; Karplus, M. The Topology of Multidimensional Potential Energy Surfaces: Theory and Application to Peptide Structure and Kinetics. *J. Chem. Phys.* **1997**, *106*, 1495–1517.
44. Fa, W.; Dong, J. Possible Ground-State Structure of Au_{26}: A Highly Symmetric Tubelike Cage. *J. Chem. Phys.* **2006**, *124*, 114310-1–114310-4.
45. Tian, D.; Zhao, J. Competition among fcc-like, Double-Layered Flat, Tubular Cage, and Close-Packed Structural Motifs for Medium-Sized Au_n ($n = 21-28$) Clusters. *J. Phys. Chem. A* **2008**, *112*, 3141–3144.
46. Perdew, J. P.; Burke, K.; Ernzerhof, M. Generalized Gradient Approximation Made Simple. *Phys. Rev. Lett.* **1996**, *77*, 3865–3868.
47. Weitao, R. G. P.; Yang *Density-Functional Theory of Atoms and Molecules*; Oxford University Press, 1994.
48. Sadeghi, A.; Ghasemi, S. A.; Schaefer, B.; Mohr, S.; Lill, M. A.; Goedecker, S. Metrics for Measuring Distances in Configuration Spaces. *J. Chem. Phys.* **2013**, *139*, 184118-1–184118-11.
49. De, S.; Willand, A.; Amsler, M.; Pochet, P.; Genovese, L.; Goedecker, S. Energy Landscape of Fullerene Materials: A Comparison of Boron to Boron Nitride and Carbon. *Phys. Rev. Lett.* **2011**, *106*, 225502-1–225502-4.
50. Huang, W.; Wang, L. S. Au_{10}^-: Isomerism and Structure-Dependent O_2 Reactivity. *Phys. Chem. Chem. Phys.* **2009**, *11*, 2663–2667.
51. Valiev, M.; Bylaska, E.; Govind, N.; Kowalski, K.; Straatsma, T.; Van Dam, H.; Wang, D.; Nieplocha, J.; Apra, E.; Windus, T.; de Jong, W. NWChem: A Comprehensive and Scalable Open-Source Solution for Large Scale Molecular Simulations. *Comput. Phys. Commun.* **2010**, *181*, 1477–1489.
52. Perdew, J. P.; Ernzerhof, M.; Burke, K. Rationale for Mixing Exact Exchange with Density Functional Approximations. *J. Chem. Phys.* **1996**, *105*, 9982–9985.
53. Zhao, Y.; Truhlar, D. G. The M06 Suite of Density Functionals for Main Froup Thermochemistry, Thermochemical Kinetics, Noncovalent Interactions, Excited States, and Transition Elements: Two New Functionals and Systematic Testing of Four M06-Class Functionals and 12 Other Functionals. *Theor. Chem. Acc.* **2007**, *120*, 215–241.
54. Perdew, J. P.; Ruzsinszky, A.; Tao, J.; Staroverov, V. N.; Scuseria, G. E.; Csonka, G. I. Prescription for the Design and Selection of Density Functional Approximations: More Constraint Satisfaction with Fewer Fits. *J. Chem. Phys.* **2005**, *123*, 062201-1–062201-9.
55. Ferrighi, L.; Hammer, B.; Madsen, G. K. H. 2D-3D Transition for Cationic and Anionic Gold Clusters: A Kinetic Energy Density Functional Study. *J. Am. Chem. Soc.* **2009**, *131*, 10605–10609.
56. Mantina, M.; Valero, R.; Truhlar, D. G. Validation Study of the Ability of Density Functionals to Predict the Planar-To-Three-Dimensional Structural Transition in Anionic Gold Clusters. *J. Chem. Phys.* **2009**, *131*, 064706-1–064706-5.
57. Taylor, K. J.; Pettiette-Hall, C. L.; Cheshnovsky, O.; Smalley, R. E. Ultraviolet Photoelectron Spectra of Coinage Metal Clusters. *J. Chem. Phys.* **1992**, *96*, 3319–3329.
58. Eyring, H. The Activated Complex in Chemical Reactions. *J. Chem. Phys.* **1935**, *3*, 107–115.
59. Genovese, L.; Neelov, A.; Goedecker, S.; Deutsch, T.; Ghasemi, S. A.; Willand, A.; Caliste, D.; Zilberberg, O.; Rayson, M.; Bergman, A.; *et al.* Daubechies Wavelets as a Basis Set for Density Functional Pseudopotential Calculations. *J. Chem. Phys.* **2008**, *129*, 14109-1–14109-14.
60. Sicher, M.; Mohr, S.; Goedecker, S. Efficient Moves for Global Geometry Optimization Methods and their Application to Binary Systems. *J. Chem. Phys.* **2011**, *134*, 044106-1–044106-7.
61. Jensen, F. *Introduction to Computational Chemistry Computational Chemistry*; Wiley: New York, 2007.
62. Roy, S.; Goedecker, S.; Hellmann, V. Bell-Evans-Polanyi Principle for Molecular Dynamics Trajectories and Its Implications for Global Optimization. *Phys. Rev. E* **2008**, *77*, 056707-1–056707-5.
63. Hartwigsen, C.; Goedecker, S.; Hutter, J. Relativistic Separable Dual-Space Gaussian Pseudopotentials From H to Rn. *Phys. Rev. B* **1998**, *58*, 3641–3662.
64. Krack, M. Pseudopotentials for H to Kr Optimized for Gradient-Corrected Exchange-Correlation Functionals. *Theor. Chem. Acc.* **2005**, *114*, 145–152.
65. Blum, V.; Gehrke, R.; Hanke, F.; Havu, P.; Havu, V.; Ren, X.; Reuter, K.; Scheffler, M. *Ab initio* Molecular Simulations with Numeric Atom-Centered Orbitals. *Comput. Phys. Commun.* **2009**, *180*, 2175–2196.
66. Zhao, Y.; González-Garca, N.; Truhlar, D. G. Benchmark Database of Barrier Heights for Heavy Atom Transfer, Nucleophilic Substitution, Association, and Unimolecular Reactions and Its Use to Test Theoretical Methods. *J. Phys. Chem. A* **2005**, *109*, 2012–2018.
67. Andersson, S.; Grüning, M. Performance of Density Functionals for Calculating Barrier Heights of Chemical Reactions Relevant to Astrophysics. *J. Phys. Chem. A* **2004**, *108*, 7621–7636.
68. Grüning, M.; Gritsenko, O. V.; Baerends, E. J. Improved Description of Chemical Barriers with Generalized Gradient Approximations (GGAs) and Meta-GGAs. *J. Phys. Chem. A* **2004**, *108*, 4459–4469.
69. Zupan, A.; Burke, K.; Ernzerhof, M.; Perdew, J. P. Distributions and Averages of Electron Density Parameters: Explaining the Effects of Gradient Corrections. *J. Chem. Phys.* **1997**, *106*, 10184–10193.
70. Ghasemi, S. A.; Amsler, M.; Hennig, R. G.; Roy, S.; Goedecker, S.; Lenosky, T.; Umrigar, C. J.; Genovese, L.; Morishita, T.; Nishio, K. Energy Landscape of Silicon Systems and Its Description by Force Fields, Tight Binding Schemes, Density Functional Methods, and Quantum Monte Carlo Methods. *Phys. Rev. B* **2010**, *81*, 214107-1–214107-12.
71. Barcaro, G.; Fortunelli, A. Structure and Diffusion of Small Ag and Au Clusters on the Regular MgO (100) Surface. *New J. Phys.* **2007**, *9*, 22-1–22-17.
72. Dal Corso, A.; Pasquarello, A.; Baldereschi, A. Density-Functional Perturbation Theory for Lattice Dynamics with Ultrasoft Pseudopotentials. *Phys. Rev. B* **1997**, *56*, R11369–R11372.
73. Haas, P.; Tran, F.; Blaha, P. Calculation of the Lattice Constant of Solids with Semilocal Functionals. *Phys. Rev. B* **2009**, *79*, 85104-1–85104-10.
74. Dal Corso, A. *Ab initio* Phonon Dispersions of Transition and Noble Metals: Effects of the Exchange and Correlation Functional. *J. Phys.: Condens. Matter* **2013**, *25*, 145401-1–145401-10.
75. Järvi, T. T.; Kuronen, A.; Hakala, M.; Nordlund, K.; van Duin, A. C.; Goddard, W. A.; Jacob, T. Development of a ReaxFF Description for Gold. *Eur. Phys. J. B* **2008**, *66*, 75–79.
76. Schaefer, B.; Mohr, S.; Amsler, M.; Goedecker, S. Minima Hopping Guided Path Search: An Efficient Method for Finding Complex Chemical Reaction Pathways. *J. Chem. Phys.* **2014**, *140*, 214102-1–214102-13.
77. Miller, M.; Wales, D.; de Souza, V. *disconnectionDPS* (Fortran program, available at http://www−wales.ch.cam.ac.uk/software.html).
78. Wang, L. S.; Cheng, H. S.; Fan, J. Photoelectron Spectroscopy of Size-Selected Transition Metal Clusters: Fe_n^-, $n = 3-24$. *J. Chem. Phys.* **1995**, *102*, 9480–9493.
79. Akola, J.; Manninen, M.; Häkkinen, H.; Landman, U.; Li, X.; Wang, L. S. Photoelectron Spectra of Aluminum Cluster Anions: Temperature Effects and *ab initio* Simulations. *Phys. Rev. B* **1999**, *60*, R11297–R11300.